

1 **Ground ice estimation in permafrost samples using industrial**
2 **Computed Tomography and Multi-Sensor Core Logging and**
3 **comparison to destructive measurements**

4 Mahya Roustaei ^{1, 2*}, Joel Pumple ¹, Jordan Harvey ¹, and Duane Froese ^{1, *}

5 ¹ Department of Earth and Atmospheric Sciences, University of Alberta, Edmonton, Canada

6 ² Geotechnics Laboratory, Ghent University, Technologiepark 68, 9052 Zwijnaarde, Belgium

7 Correspondence to: Mahya Roustaei (mroustae@ualberta.ca) or Duane Froese (duane.froese@ualberta.ca)

Abstract.

Permafrost contains a variety of ground ice types (e.g., pore, segregated, intrusive, vein, or massive ice) that have a diversity of cryotextures which organise to form distinctive cryostructures. The distribution and abundance of those ground ice types determines the potential for thaw subsidence and terrain effects of permafrost landscapes. Analysis of permafrost samples allows improved understanding of ground ice formation, internal and external permafrost processes, and improved tools to predict thaw settlement and consolidation. However, most methods to characterise permafrost are destructive and of low resolution. Here, some of the limitations of traditional destructive methods are overcome using an industrial Computed Tomography scanner (CT). We use this laboratory-based method to systematically characterize five permafrost samples. We visualise cryostructures, measure frozen bulk density, and estimate volumetric and excess ice contents non-destructively and compare these results with traditional destructive analyses at similar spatial scales.

The results show strong agreement between traditional destructive analyses (RMSE's for density, VIC, and EIC are 0.12 g/cm³, 3% and 6%, respectively) as well as recent developments using a Multi-Sensor Core Logger (MSCL) (RMSE's for density and VIC are 0.08 g/cm³ and 7%, respectively). These results demonstrate that these non-destructive approaches can produce consistent results, and provide the added benefit of archiving images and enhancing digital permafrost datasets.. Development of standardised and interoperable methods for permafrost characterization has the potential to build more robust permafrost datasets and strengthen efforts to understand future thaw trajectories of permafrost landscapes.

1 Introduction

Permafrost is rock or soil that has remained below 0°C for at least two consecutive years. Within permafrost, several different types of ground ice can form: pore ice within the void spaces between soil or rock particles; segregation ice as distinct lenses formed through migration of water within permafrost; aggradational ice, a type of segregation ice, that forms as the permafrost table rises; vein or wedge ice that forms within thermal contraction cracks; intrusive ice that forms when water is injected under pressure; or massive ice that refers to relatively pure bodies of ice within permafrost. (Subcommittee on Permafrost, 1988). These differing types of ground ice have distinctive associations of cryotextures, which refer to the appearance and characteristics of ice crystals, gas bubbles and their interfaces with soil particles at a more microscopic scale; and cryostructures which refer to the three-dimensional patterns and arrangements of ice bodies within the frozen ground (such as layered, lenticular, or reticulate patterns) (Murton and French, 1994; French and Shur, 2010). Taken together, these ice-related features help identify the genesis of perennially frozen sediments and can provide insights into the conditions under which the permafrost formed, which can aid in understanding potential ground ice distribution. Of particular importance is excess ice – or ground ice that exceeds the natural pore volume that the sediment would have under unfrozen conditions (Brown et al., 1997; Zhang et al., 1999; Cai et al., 2020; Van Everdingen, 1998). When excess ice melts, it causes thaw settlement and ground subsidence, making its quantification increasingly critical as warming temperatures degrade permafrost across permafrost regions (e.g. Kokelj et al., 2024). Projections of widespread permafrost thaw by the end of this century (e.g. Cai et al., 2020) highlight an urgent need for standardised methods to measure and map excess ice distribution to better predict future landscape change.

Cryostructural approaches to ground ice classification, building on Russian literature, particularly Katasonov's (1969, 1978) cryofacies methods, focus on understanding permafrost genesis and development through systematic analysis of the shape, size and spatial patterns of ice inclusions in frozen ground. This approach contrasts with the more commonly used North American engineering-focused descriptive systems developed by Pihlainen and Johnston (1963) and Johnston (1981), which rely primarily on visual descriptions and simple field tests, such as thawing samples to observe supernatant water content similar to the method described in Kokelj and Burn (2003). While the descriptive approach provides practical field-based classifications useful for engineering applications, the cryostructural approach offers more process-based insight into permafrost formation processes and potential ground ice distribution, which is increasingly important for predicting thaw settlement and landscape response to climate warming.

Traditional approaches to permafrost characterization, whether using more descriptive engineering-oriented approaches (Pihlainen and Johnston, 1963; Johnston, 1981) or more detailed cryostructural classifications (Murton and French, 1994; French and Shur, 2010), rely heavily on visual description of exposures and cores (Kanevskiy et al., 2011; Stephani et al., 2014). While these approaches have advanced our understanding of permafrost, they require substantial experience of the

analyst, and are difficult to standardise. Quantitative methods typically require destruction of samples to measure ice and moisture contents, which works well for ice-rich mineral soils but presents challenges for organic-rich materials where water may be retained in thawed samples. These limitations have driven the development of non-destructive methods like Computed Tomography (CT) scanning that can systematically analyse intact frozen cores, providing standardised, quantitative data on ground ice while preserving samples for additional analyses. This approach offers the potential to better understand permafrost formation, internal structure, and likely response to thaw while developing more consistent and interoperable methods applicable across different permafrost materials.

Micro-computed tomography (μ CT) has emerged as a promising solution to the limitations of traditional permafrost characterization methods since the pioneering work of Calmels and Allard (2004, 2008), who demonstrated its utility for measuring ice and gas contents in permafrost and linking these to processes of ground ice formation. Subsequent studies have expanded the application of CT scanning to examine cryostructures (Calmels et al., 2010; Fan et al., 2021), excess ice (Lapalme et al., 2017), soil degradation in freeze-thaw cycles (Nguyen et al., 2019; Wang et al., 2018, 2017; Roustaei et al., 2022), quantification of micro-lenticular ice lens formation (Darrow and Lieblappen, 2020), unfrozen water content (Roustaei et al., 2022), soil-ice relations (Torrance et al., 2008), and permafrost composition (Nitzbon et al., 2022).

However, despite these advances, there have been few systematic comparisons of high-resolution CT scanning ($< 100 \mu\text{m}$) with established methods for differentiating excess ice from pore ice across different permafrost materials. This study addresses this gap by using industrial CT scanning, which offers higher peak power and resolution than medical CT scanners, to analyse five different permafrost cores representing a range of typical properties. We develop a new approach using an internal water standard to calibrate linear attenuation coefficients to real density values, and systematically compare CT-derived measurements of frozen bulk density, excess ice, and volumetric ice contents with both destructive physical measurements and Multi-Sensor Core Logging (MSCL) results from Pumple et al. (2023). We include a sensitivity analysis to examine how spatial resolution affects excess ice estimation. While our sample set does not capture the full heterogeneity of permafrost materials and ground ice abundance, it provides a rigorous test of CT methods for quantifying ground ice in common permafrost materials, with the goal of developing more robust and standardised approaches for permafrost characterization and mapping.

Cryostructural approaches to ground ice classification build on earlier Russian literature, particularly Katasonov's (1969, 1978) cryofacies methods, which established relationships between the shape, size and spatial patterns of ice inclusions in soils (i.e.,

eryostructures) to understand permafrost formation and development. These methods helped establish links between eryostructures and specific terrain units.

An important property of permafrost is the presence of excess ice, or ice that exceeds the total pore volume that the ground would have under unfrozen conditions (Brown et al., 1997; Zhang et al., 1999; Cai et al., 2020; Van Everdingen, 1998). Eis called *excess ice* and can affect the permafrost thermal regime (in form of phase composition along with other permafrost components), landscape structure, and the amount of thaw settlement following disturbance (Schramm and Becht, 2019). Widespread thawing of permafrost is expected under a warmer future climate and modelling studies suggest large-scale degradation of near-surface permafrost by the end of this century (Lawrence et al., 2008, 2011; Cai et al., 2020). Past studies have illustrated that the presence of excess ice and its distribution in permafrost can significantly affect the impact the rates of permafrost thaw and consequently Arctic ecosystems (Kokelj and Jorgenson, 2013; Westermann et al., 2016; Nitzbon et al., 2020). A better estimation of ground ice distribution and abundance is important for improving existing methods for mapping the distribution of excess ice at landscape scales, and predicting the impacts of permafrost thaw (Cai et al. 2020).

A recognized standard should be used in field and laboratory tests for description of ground ice and excess ice estimation. Katasonov (1969, 1978) offered a cryofacies method for estimating ice distribution of permafrost based on a close relationship between the shape, size, and spatial pattern of ice inclusions in soils (i.e., eryostructures) and specific terrain units. to understand ground ice genesis, and reveals the nature of permafrost formation. Philainen and Johnston (1963) and Linell and Kaplar (1966) have created a descriptive system that is used widely in geotechnical descriptions of permafrost in North America (ref ASCE or equivalent?). North America.

The main description procedure of this method is visual, accompanied by simple field tests and in some cases more explicit description. The simple field test which is suggested to aid evaluation of volume of excess ice includes placing some frozen soil in a small jar and observing the quantity of supernatant water after thaw. The estimated volume of visible segregated ice is defined as a percentage of the total sample volume in addition to a descriptive term showing hardness (e.g., hard or soft), structure (e.g., clear, cloudy, porous, candled, granular, or stratified), colour (e.g., grey or blue), and admixtures.

Descriptive systems have been used widely in North America for field and laboratory tests for description of ground ice and excess ice estimation (Philainen and Johnston, 1963; Linell and Kaplar, 1966). These approaches are largely visual, accompanied by simple field tests and in some cases more explicit descriptions. One simple field test that has been used to aid the evaluation of excess ice volume involves placing frozen soil in a small container and observing the quantity of supernatant water after thaw.

Besides the differences in estimates from these visual methods descriptions, observers may be misled by surface scratches or frost coating on cores the ice (Johnston, 1981). In addition, visual estimates of excess ice are deceptive because sediment may not necessarily contain excess ice, even though it may contain visible ice lenses. This is because the sediment

surrounding the lenses may not be saturated with ice and upon thaw, water is retained in voids or by hosted organic matter (French, 2018).

Visual description of exposures and drill cores is also the most common typical method for cryostructural characterization (e.g. Kanevskiy et al., 2011; Kanevskiy et al., 2012; Stephani et al., 2014). Others are done by sampling and surficial geology mapping (Kokelj and Burn, 2003; O'Neill and Burn, 2012), or by geophysical and airborne methods (Jorgenson et al., 2003; Gilbert et al., 2016; Schramm and Becht, 2019). Traditional quantitative characterization methods mostly involve destruction of permafrost cores to extract the supernatant water and gravimetric moisture contents. These methods work well for ice-rich uniform mineral soils but have limitations for soils with high organic contents. Considering the limitations of visual and experimental methods of ground ice classification and excess ice measurements, as well as different sample sizes and levels of resolution in these methods, there is a need to develop consistent and interoperable methods for ground ice classification and estimation applicable for all types of sediments.

Being able to analyse frozen, undisturbed, cores of permafrost allows one to better understand how it formed, internal transforming processes of permafrost and to predict the amplitude of thaw settlement and consolidation.

Over the last few several decades there have been rapid advances in the use of non-destructive methods for the investigation of internal textures and physical properties of frozen materials (e.g., ice content, density and thermal conductivity). These techniques enable researchers to analyse frozen and undisturbed permafrost cores to find a better understanding of the ice formation and also the internal transformation processes to well predict the amplitude of thaw settlement and consolidation.

One of these techniques is micro-computed tomography (μ CT) which has been a useful tool in permafrost research since the initial studies by Calmels and Allard (2004, 2008). They used CT to measure ice and gas contents in ice-rich permafrost and established links between permafrost landforms and various cryostructures associated with the ice segregation process/microscale cryostructures. Recent works have focused on cryostructures (Calmels et al., 2010; Fan et al., 2021), excess ice determination (Lapalme et al., 2017), distribution and consolidation of soil between ice lenses (Torrance et al., 2008), soil degradation in freeze-thaw cycles (Nguyen et al., 2019; Wang et al., 2018, 2017; Roustaei et al., 2022), quantification of micro-lenticular ice lens formation (Darrow and Lieblappen, 2020), unfrozen water content (Roustaei et al., 2022), thermal conductivity (Ducharme et al., 2015), quantifying freezing processes in a clayey soil (Amato et al., 2022) and composition and microstructural investigation of permafrost (Nitzbon et al., 2022). Although these studies demonstrate the application of CT in estimating the ground ice contents of permafrost cores and illustrating the cryostratigraphical differences, there are very few investigations on differentiating excess ice and pore ice contents via very high-resolution scans (less than 100 μ m) in different types of permafrost samples and comparing these data to established methods at similar spatial scales.

So this study highlights the application of uses CT imaging as a non-destructive method to tackle the limitations of traditional ground ice quantification classification methods and previous works by measuring frozen bulk density and estimating not only the excess ice and volumetric ice contents quantitatively but also measuring frozen bulk density from five different permafrost samples at a high spatial resolution. The permafrost cores in this study do not represent the entire berth of heterogeneity encountered in all permafrost impacted landscapes but instead act as a starting point to test this non-destructive CT method for estimating ice contents within permafrost core materials. The CT scanner used in this study is a cabinet-based industrial CT scanner commonly used in the automotive and manufacturing industries. The main difference between an industrial μ CT scanner and a medical CT scanner is the higher peak energy power (greater penetration potential) and higher image resolution (voxel size) of the industrial μ CT scanner. A new approach is also implemented for collecting CT scans with an internal standard (water) later used to calibrate the resulting linear attenuation coefficients into real density (g/cm^3), see Sect. 2.3.1 for more details. All CT density and volumetric ice content results are compared to a recent study using the same cores but a different non-destructive method, MSCL (Pumple et al., 2024), and the advantages of each are discussed similarly to Fortin et al., (2013), but instead focused on permafrost materials. Finally, a quantitative comparison between the excess ice results collected via physical measurements the destructive cuboid method and the CT image analysis is presented to show the reliability of the methods, including a sensitivity analysis to illustrate the effect of spatial resolution on excess ice estimations. The results of this study could help build more robust permafrost datasets and strengthen future efforts to map permafrost terrains and establish thaw sensitivity at the regional scale.

2 Methods and Materials

2.1 Field site and coring Materials

Five cores were compared in this study, each representing common materials encountered in permafrost regions and containing a relatively simple vertical cryostratigraphy to minimize the impact of lateral heterogeneity (Table 1). Lateral heterogeneity would cause noise in our results when comparing multiple data acquisition methods within the same material but not identical sample volumes (Figure 1). This effort is explained further by Pumple et al. (2024). These cores were collected as a result of two separate field campaigns during the summers of 2013 and 2019. Following extraction, the cores were bagged, labelled and stored at subzero temperatures via a pre chilled cooler and quickly transported to the field base where a chest freezer was present. The chest full of cores was then transported to the Permafrost ArChives Science (PACS) Laboratory. The samples were then archived into the PACS Lab walk-in archive freezer space. PACS Laboratory hosts a specialized imaging space where both the Nikon XTH 225 ST and the Geotek multi-sensor core logger (Pumple et al., 2024) are located. The imaging space is kept at 23 °C and as a result, special consideration has to be taken when working with frozen materials. An insulated sample container was used to keep the samples frozen during the scanning process which is discussed further in section 2.3.5.

181 **2.2 Sampling Process**

182 In this study the samples were prepared for two The sample preparation process of this off for this study consisted of different
183 stages; non-destructive scans and destructive physical measurements. We took consideration took needed considerations in
184 both stages to ensure the destructive and non-destructive results were comparable. As such for the non destructive scans,
185 physical cores were cut in half and run through all non-destructive data collection methods, prior to subsampling. For the
186 second stage, During subsampling, a duplicate transect of the cuboid samples was collected from the middle of the core to
187 allow non-destructive data analysis at a higher resolution on one set of the subsampled cubes. As seen in Figure 1, this resulted
188 in the cuboids flanking either side of the MSCL and CT results which were collected from a central transect on the half-core
189 samples.

190 **2.3 Physical Density Measurements**

191 Ground ice content is typically expressed either as the gravimetric moisture/ice content (the ratio of the mass of the ice in a
192 sample to the mass of the dry sample) or the volumetric moisture/ice content (the ratio of the volume of ice in a sample to the
193 volume of the whole sample) (Van Everdingen, 1998). Similar to thaw strain measurements in geotechnical investigations
194 (Crory, 1973; Shur, 1988; Pullman et al., 2007; Kanevskiy et al., 2012), Kokelj and Burn (2003) and O'Neill and Burn (2012)
195 both applied a method for destructively extracting excess ice content measurements from frozen samples. This method includes
196 the complete thaw, homogenization, and settling time of the sample to extract the supernatant water content and estimate
197 excess ice content. Their method does not require measurement of frozen sample volume since the volumes of sediment as
198 well as the supernatant water should be recorded from the beakers containing the samples once completely thawed. The excess
199 ice content (E_i) of the samples can then be estimated by the equation (Kokelj and Burn, 2003):

200
$$(E_i) = \frac{(Wv + 1.09)}{(Sv + Wv + 1.09)} * 100 \quad (1)$$

201 Where Wv is the volume of supernatant water (cm^3), multiplied by 1.09 to estimate the equivalent volume of ice, and Sv is the
202 volume of saturated sediment (cm^3).

203 This study takes an approach similar to Kokelj and Burn (2003) in that the supernatant moisture content is
204 destructively assessed in order to calculate excess ice content. However, since the volume of soil samples was precisely
205 measured in this study using the cuboid method, volumetric ice contents were also measured. Because in some soils, such as
206 peat, excess ice will be absorbed by the soil skeleton upon thaw (Johnston, 1981), the Kokelj and Burn method was adjusted
207 for samples with high organic contents by applying a slight pressure on the thawed cube and extraction of the released
208 water. Additionally, the organic content of each sample was measured via loss on ignition (LOI) (Heiri et al., 2001). The
209 cuboid method, described by Bandara et al. (2019), is similar to other volumetric and gravimetric methods used to measure
210 bulk density (particularly peat deposits) and ice content, but takes advantage of the ice rich properties of frozen cores which

allow for a greater degree of sampling precision. Processing is undertaken in a walk-in freezer following methods outlined in Pumple et al. (2023).

2.4 Multi Sensor Core Logger (MSCL)

The PACS Laboratory MSCL is a floor mounted, automated logging system, manufactured by Geotek, which can be used to analyse whole or split cores. This core logger is equipped with two magnetic susceptibility instruments, a line scan camera, and a Caesium 137 (^{137}Cs) gamma source and detector which provides measurements of gamma attenuation. Pumple et al. (2023) provides additional details on the methods used for the MSCL data collection and calibration. The combination of the frozen bulk density results from the gamma attenuation, an estimation of soil density, and the equation presented for volumetric ice content, following Lin et al. (2020), can be used to estimate non-destructively using the MSCL (Pumple et al., 2023).

2.3.5 Industrial Micro Computerized Tomography

Micro Computed tomography (μCT) was used to examine the ice, sediment, and gas contents of several permafrost cores and cube samples. This method is a non-destructive technique that has been useful in the investigation of geological porous media (Ashi, 1997; Ketcham and Carlson, 2001; Kozaki et al., 2001; Flisch and Becker, 2007; Calmels and Allard, 2004; Van Geet et al., 2005; Tanaka et al., 2010; Nitzbon et al., 2020). This imaging method captures radiograph images through the production of x-rays which pass through the cabinet and are recorded by the detector panel opposite the source. The sample is placed between the source and the detector panel and the resulting relative absorption of the x-rays energy is recorded by the detector panel creating the radiograph image. To collect a 3 dimensional image it consists firstly in recording a set of two-dimensional X-ray radiographs are collected at multiple angles, and secondly reconstructing the 2D slices to form a 3D image using a mathematical algorithm. The final measurement unit which is commonly visualised presented in a histogram the histogram is the linear attenuation coefficient which depends on both the density and the electron density of the material (Ketcham and Carlson, 2001). This study differs slightly from earlier permafrost CT studies that report values in Hounsfield units that are common in medical CT studies (eg. Calmels et al., 2010). In this study, an internal calibration process is used to convert the primary linear attenuation values derived from the CT data directly to density (g/cm^3).

The scans presented here were captured using a helical scan with a Nikon XTH 225 ST cabinet-based industrial computed tomography micro-CT scanner. The system uses an electronically adjustable 225Kv 225W power source (Figure 2). This system includes both a tungsten rotating reflection target source and a tungsten fixed reflection target source coupled with a 16-bit 2000x2000 pixel detector capable of a focal spot size range of 3-121 μm depending on the size of the area of interest and size of the object being scanned. The 10 cm diameter frozen permafrost half cores were scanned with the reflection target source at 200 Kv 35 μA with an exposure time of 125 ms and a voxel (3D volume element representing pixel resolution and slice thickness) size of 65 μm . Scan times ranged from 30 to 45 minutes per core, with a maximum height of ~12 cm scanned per core due to vertical stage movement limitations and inclusion of calibration materials. The subsampled cubes from

the cores were scanned with the rotating reflection target source at 225 Kv 133 μ a with an exposure time of 125 ms and a voxel size of 25 μ m. Scan times for the subsampled cubes were 30 minutes per cuboid. The images were reconstructed into three-dimensional grey-scale volumes using the Nikon CT pro 3D software and analyzed using ORS Dragonfly 2022 image processing software (ORS 2021).

This project was completed during development of an insulated sample holder for use in the CT scanner. Both cubes and cores were housed in the same style of a styrofoam container, however, the internal setup varied due to the size of the sample under investigation. Cores were taken from a nearby chest freezer, quickly placed in a larger styrofoam container with an inner diameter of 12 cm in the vertical position and an ice pack was placed directly above them (Figure 2B and C). For this experiment, all ice packs were cooled to -80 C prior to being added to the container at the start of the scan. The ice packs held the core's surface temperature below freezing for the duration of the scan. The cubes were held in a slightly smaller container with an inner diameter of 9 cm in a small plastic vial with a foam divider directly above (Figure 2D). The cubes were cooled with a small amount of dry ice placed on a perforated foam divider to bathe the underlying sample with cold air during scanning. Both setups are able to hold the core's surface temperatures below freezing for the full duration of the scan time.

It should also be noted that the partial results for most full cores are due to a height restriction encountered during the helical scans. Although the CT scanner can hold samples up to ~ 30 cm wide by 35 cm high, the area that is able to be scanned is dependent on the desired voxel size and the width of the sample. This restriction was resolved after cores were subsampled for the destructive cuboid method. This means for some of the cores we were unable to compare the complete vertical data sets of the MSCL, destructive cuboid, and CT results (e.g. peat core).

2.3.1.6 CT Calibration

The linear attenuation coefficient (μ) represents the energy attenuated within a single voxel volume while the voxel population is the population of voxels within a scan volume (Ketcham & Carlson, 2001). By creating a histogram (linear attenuation coefficient vs voxel population) with these μ -values from each sample, distributions of relative grey values can be presented. If uncalibrated, the resulting grey values observed in the histogram of a CT scan appear as linear attenuation coefficients. The medical field has developed methods for converting linear attenuation coefficients to Hounsfield units and as a result, the Hounsfield unit has become commonly used in CT research (Hounsfield, 1973; Wellington and Vinegar, 1987; Dului, 1999; Knoll, 2000; Ketcham and Carlson, 2001; Duchesne et al., 2009). Lee et al., 2015 took it one step further and converted mean Hounsfield unit values to bone mineral density values (mg/cm^3) via a linear regression analysis. A similar approach was used in this study by collecting the CT scans with an internal standard of known density (water) later used to calibrate the resulting linear attenuation coefficients into g/cm^3 using the Nikon CT Pro 3D software. It should be noted that all cores were scanned with ice, water, and aluminum calibration pieces of which water proved to be in closest agreement with destructive analyses. The water and aluminum were located outside of the insulated container during the core scans to avoid freezing. The cube scans had only the water located directly above the cube sample but isolated from the sample and dry ice by insulated foam to

minimize the exposure to the cold air temperature within the insulated container. The aluminum calibration piece generally underestimated the bulk density while the ice calibration piece resulted in a slight overestimation. Aluminum was chosen for its consistent density of 2.71 g/cm³ representing an upper limit of the expected bulk density within the selected materials. The ice calibration was a 15 ml falcon tube filled and frozen at -5°C to minimize expansion issues and bubbles. Overall the water calibration produced the most accurate results apart from ice-poor sediments. The Nikon CT Pro 3D software uses a linear two-point calibration with the first fixed point being air (equal to zero) and the second a user-defined value based on a user-selected pixel population. A representative (local) population of pixels was selected from our water sample in a 2D slice of the scan and informed the expected average target value (1 g/cm³). This results in the histogram displaying grey values in g/cm³. These densities can then be presented in a histogram where the shape of the histogram changes with the proportion of the component materials and thus approximates the volumetric content in a sample (Calmels et al. 2010).

2.3.27. Image Processing

Image preprocessing usually consists of two main stages: 1) selection of the Region of Interest or (ROI), 2) segmentation. In this study both stages were done using and four steps. This study uses Dragonfly software (ORS 2021). This software enabled us to process the three-dimensional reconstructed X-ray tomographs of the frozen materials to segment, quantify, calculate, and illustrate the cores materials' physical properties. For the first stage, a series of ROIs were created in the half core CT results down the central vertical axis of the cores to mimic the data collection points of the MSCL as presented in Pumple et al. (2024). Figure 1 displays the relative location of these ROIs which were sized to match the spot size of the gamma-ray at the surface of the core, ~10 mm in diameter. The central point of each ROI was placed 5 mm apart resulting in a significant overlap between adjacent data points, again similar to the data collection process for the MSCL. In this study, all cores were calibrated so the histogram values were displayed in g/cm³. To extract the frozen bulk density from each ROI, the mean grey values were extracted in calibrated density values (g/cm³).

The second stage, segmentation or the ability to differentiate materials, depends on their respective linear attenuation coefficients, meaning materials with divergent densities and/or atomic numbers are easier to differentiate (Kyle and Ketcham, 2015). Analysing a multi-modal histogram of a CT image is straightforward for material differentiation while materials with narrow unimodal density distributions close densities appear as a single peak in the histogram. In addition to the relative density of the scanned materials, the image resolution or voxel size also directly impacts the image segmentation process. The voxel size can impact the image segmentation through the partial volume effect which relates directly to the finite spatial resolution or voxel size of the scan and for geological samples, grain size, minimal pore size, and organic content, the grain size distribution (Soret et al., 2007; Nitzbon et al., 2022).

In this study, an automatic image thresholding method named "Otsu" was used. One of the main Dragonfly software features utilized in this study is the Otsu image thresholding method. The algorithm of this method, proposed by Nobuyuki Otsu (1979), performs automatic clustering-based image thresholding. In this method, it is assumed that there are two classes of

pixels which are “foreground” and “background” pixels of the image. The optimum thresholding is calculated by distinguishing the two classes so that the minimum class variance is obtained (Kumar and Tiwari, 2019). This method was applied to the selected regions of interest from stage one to differentiate sediment and ice. In each image processing step, we tried This allows us to isolate the materials within our scans based on density and slowly slice away the lighter density portion (ice) until we are certain we have collected the target material range (often a mixture of ice and sediment). Figure 3 shows the ice (less dense material) being segmented from the surrounding sediment through multiple image processing steps using the Otsu method where only the background (less dense) portion of the previous step is added to the final result. This approach shows that applying the first image processing step will mainly extract the visible ice while using multiple Otsu analyses additional lower-density ice-rich mixtures (mainly pore ice) are extracted, e.g., the area shown inside the red circle of Figure 3B-D. Note that all the above mentioned segmentation steps can also be done by visual inspections instead of automatic thresholding method but it can vary significantly between users, leading to inconsistent results.

2.3.38 Region of Interest (ROI)

A series of ROIs were created in the half core CT results down the central vertical axis of the cores to mimic the data collection points of the MSCL as presented in Pumple et al., 2023. Figure 1 displays the relative location of these ROIs which were sized to match the spot size of the gamma ray at the surface of the core, 10 mm in diameter. The central point of each ROI was placed 5 mm apart resulting in a significant overlap between adjacent data points, again similar to the data collection process for the MSCL. In this study, all cores were calibrated so the histogram values were displayed in g/cm³. To extract the frozen bulk density from each ROI, the mean grey values were extracted in calibrated density values (g/cm³).

2.4 Physical Density Measurements

Ground-ice content is typically expressed either as the gravimetric moisture/ice content (the ratio of the mass of the ice in a sample to the mass of the dry sample) or the volumetric moisture/ice content (the ratio of the volume of ice in a sample to the volume of the whole sample) (Van Everdingen, 1998) while excess ice refers to the amount of ice in the soil that exceeds the volume of the pore space in the unfrozen state. Similar to thaw-strain measurements in geotechnical investigations (Crory, 1973; Shur, 1988; Pullman et al., 2007; Kanevskiy et al., 2012), Kokelj and Burn (2003) and O'Neill and Burn (2012) both applied a method for destructively extracting excess ice content measurements from frozen samples. This method includes the complete thaw, homogenization, and settling time of the sample to extract the supernatant water content and estimate excess ice content. Their method does not require measurement of frozen sample volume since the volumes of sediment as well as the supernatant water should be recorded from the beakers containing the samples once completely thawed. The excess ice content (Ei) of the samples can then be estimated by the equation (Kokelj and Burn, 2003):

337
$$(Ei) = \frac{(Wv \times 1.09)}{(Sv + Wv \times 1.09)} * 100 \tag{1}$$

338 where Wv is the volume of supernatant water (cm3), multiplied by 1.09 to estimate the equivalent volume of ice, and Sv is the
339 volume of saturated sediment (cm3).

340 This study takes an approach similar to Kokelj and Burn (2003) in that the supernatant moisture content is
341 destructively assessed in order to calculate excess ice content. However, since the volume of soil samples was precisely
342 measured through the following steps (Pumple et. al, 2024), volumetric ice contents were also measured.

343 To independently assess density and ice content measurements and also being able to perform scans at higher
344 resolutions, the cores were subsampled as 2x2x4cm cubes. The subsampling process was done in a walk-in freezer maintained
345 at -7°C. The initial step involved removing material from the outer edges of the whole core that might have thawed during
346 coring or been affected by sample storage. Core segments were split lengthwise with a rock saw equipped with a 35 cm
347 diameter diamond-cutting wheel. Cuboid aliquots were cut from one half of the split core, while the other half was retained as
348 an archive. The rounded edges were removed from the half core to expose an internal slab. For this study, a duplicate set of
349 cuboids was obtained by cutting the internal slab in half. Approximately 3 cm³ aliquots were subsampled from the cores to
350 ensure that the cuboids did not fracture or disintegrate during sampling due to the lower ice content. Digital calipers (+0.01
351 mm) and a digital analytical balance (+0.01 g precision) were used to measure physical dimensions and mass, respectively, to
352 calculate the frozen bulk density. The cuboids were then thawed at room temperature for 24 hours in glass beakers covered
353 with Parafilm to minimize evaporative loss. Excess moisture was removed from the beakers containing the thawed samples,
354 and the sample weight was recorded again to calculate excess moisture content. The cuboids were then dried in an oven for 24
355 hours at 105°C and reweighed to determine both volumetric ice content and gravimetric moisture content. Finally, the
356 remaining dried material was heated at 550°C for 4 hours to determine the percent organic content via loss on ignition. High
357 organic content could result in water absorption by soil matrix upon thaw and more complexity in measuring excess ice
358 contents.

359 Because in some soils, such as peat, excess ice will be absorbed by the soil skeleton upon thaw (Johnston, 1981), the
360 Kokelj and Burn method was adjusted for samples with high organic contents by applying a slight pressure on the thawed cube
361 and extraction of the released water. Additionally, the organic content of each sample was measured via loss on ignition (LOI)
362 (Heiri et al., 2001). The cuboid method, described by Bandara et al. (2019), is similar to other volumetric and gravimetric
363 methods used to measure bulk density (particularly peat deposits) and ice content, but takes advantage of the ice-rich properties
364 of frozen state cores of the material which allows for a greater degree of sampling precision. Processing is undertaken in a
365 walk-in freezer following methods outlined in Pumple et al. (2024).

366 2.5 Multi Sensor Core Logger (MSCL)

367 The PACS Laboratory MSCL is a floor-mounted, automated logging system, manufactured by Geotek, which can be used to
368 analyse whole or split cores. This core logger is equipped with two magnetic susceptibility instruments, a line-scan camera,

and a Caesium-137 (137Cs) gamma source and detector which provides measurements of gamma attenuation. Pumple et al. (2024) provides additional details on the methods used for the MSCL data collection and calibration. The combination of the frozen bulk density results from the gamma attenuation, an estimation of soil density, and the equation presented for volumetric ice content, following Lin et al. (2020), can be used to estimate non-destructively using the MSCL (Pumple et al., 2024).

3 Results and Discussions

3.1 Image Segmentation

In CT, the ability to differentiate materials depends on their respective linear attenuation coefficients, meaning materials with divergent densities and/or atomic numbers are easier to differentiate (Kyle and Ketcham, 2015). Analysing a multi-modal histogram of a CT image is straightforward for material differentiation while materials with narrow unimodal density distributions close densities appear as a single peak in the histogram. In addition to the relative density of the scanned materials, the image resolution or voxel size also directly impacts the image segmentation process. The voxel size can impact the image segmentation through the partial volume effect which relates directly to the finite spatial resolution of the scan and for geological samples, the grain size distribution (Soret et al., 2007; Nitzbon et al., 2022).

Figures 4 A and B show one slice of a small ROI and its histogram from 5 different cores of this study. The differences in the shapes of the histograms are due to the different sediment densities. The diamicton core has the highest sediment density and a bimodal histogram in which the first mode represents ice and the second is related to the sediments and clasts. Whereas in the other cores, ice and sediment appear as a single mode. Image segmentation of these slices using the Otsu method resulted in the differentiation of 5 different classes of ice/sediment ratios materials on the basis of their relative densities; air, low ice, high ice, low sediment, and high sediment shown in Figures 4 B and C. Low ice comprises primary visual or excess ice while high ice mainly results from extraction of pore ice or ice proximal to sediment (sediment-rich ice). It should be noted that the pore ice inclusions within the mineral soil matrix are often smaller than the spatial resolution of the CT and the resulting grey value of a voxel is then a mixture of low-density ice and high-density minerals. This phenomenon, called partial volume effect, is the main reason why the high ice appears denser. Low sediment and high sediment are also differentiating ice-rich sediments and sediments with lower and higher densities, respectively. Figure 5 illustrates the image segmentation results in the whole diamicton core. These figures illustrate the effectiveness of the Otsu method in generating robust segmentation results while the visual inspection method has its own drawbacks, e.g. inspector's visual acuity and poor reproducibility.

3.1.2 Core Results

The results presented below combine the image processing analysis of CT images from 5 cores and a systematic quantitative comparison between the Cuboid (destructive method) and the recent non-destructive method presented by (Pumple et al.,

401 (20243). Physical properties of the permafrost samples, determined from the cuboids, including frozen bulk density, volumetric
402 (VIC) and excess ice contents (EIC), and organic contents are plotted versus the depth of the cores and shown as B, C, and D
403 in Figures 6-10, respectively. The vertical cross-section photo of the core (A) is also presented in these figures. The non-
404 destructive CT results for VIC, EIC, and bulk density for each core are then compared to both the destructive cuboid and non-
405 destructive MSCL results using an average root mean square error (RMSE) (Table 2).

406 **3.12.1 Ice-rich Silt Core (BH18-211):**

407 Figure 6 shows the destructive (cuboid) and non-destructive (CT and MSCL) results of the ice-rich silt core, illustrating that
408 the CT frozen bulk densities are in strong agreement with both the cuboid (RMSE = 0.12 g/cm³) and MSCL (RMSE = 0.14
409 g/cm³) results. This core has a high organic content (8-19% organic), micro-lenticular and layered cryostructures, and 66%
410 silt. Cuboid physical EIC and VIC measurements range from 19-34% and 68-76%, respectively, while the CT EIC and VIC
411 estimates range from 20-68% and 32-74% at the same depths where cuboid measurements were collected. The 65 µm EIC
412 (redline in Figure 6C) shows good accordance with the cuboid EICs (RMSE = 9%) apart from the ice layer where the cuboid's
413 relatively low sample resolution results in an averaging out of the ice content across the ice layer. ~~The MSCL results~~
414 ~~consistently display lower values relative to the cuboid data.~~ The 65 µm CT-VICs (black line in Figure 6C) illustrate the
415 resolution limitation in extracting the pore ice of this sandy silt core while the 25µm VICs shown as black cubes in the same
416 plot tackle this limitation and agree well with VICs extracted from the Cuboid method (RMSE = 7%). The MSCL VICs follow
417 the same trend as the cuboid data (Fig 6-C) but consistently tend toward lower values in the ice-poor regions.

418 **3.12.2 Transition Core (BH12F-138):**

419 Figure 7 shows the results of the transition core from both destructive (cuboid) and non-destructive (CT and MSCL) methods,
420 illustrating a sharp boundary between an ice-rich silty peat, containing massive and rare crustal cryostructures, and an ice-poor
421 inorganic silt with a mainly micro-lenticular cryostructure. The organic content of the core's top section, ranging from 53-
422 71%, highlights this transition (Figure 7D). Cuboid physical EIC and VIC measurements range from 6-28% and 64-88%,
423 respectively, while the CT EIC and VIC estimates range from 9-33% and 42-95% at the same depths where cuboid
424 measurements were collected. This figure also shows that the CT bulk density results are in strong agreement with both the
425 cuboid (RMSE = 0.13 g/cm³) and gamma attenuation data (RMSE = 0.06 g/cm³) (Pumple et al., 20243). The 65 µm EIC results
426 (red line in Figure 7-C) follow the cuboid results (RMSE = 5%) in the silty section. The 65 µm VIC (black line in Figure 7C)
427 resolves more than 50% of pore ice, while the higher resolution (25 µm, black cubes in Figure 7C), estimates up to 100%
428 (RMSE = 3%).

3.12.3 Diamicton Core (BS19-3-6):

Figure 8 illustrates the destructive (cuboid) and non-destructive (CT and MSCL) results of the diamicton core. This ice-rich diamicton contains both suspended and crustal cryostructures and more than 50% silt (Table 1). Overall the bulk density and ice measurements from CT display high concordance with the gamma attenuation ($RMSE = 0.14 \text{ g/cm}^3$), and cuboid ($RMSE = 0.14 \text{ g/cm}^3$) methods (Figure 8). Cuboid physical EIC and VIC measurements range from 30-50% and 48-66%, respectively, while the CT EIC and VIC estimates range from 22-57% and 36-77% at the same depths as the cuboid measurements. The 65 μm EIC results (red line in Figure 87C) follow the cuboid results ($RMSE = 8\%$). The only point where the datasets differ notably is at 2-4 cm depth where the MSCL ~~valuesdataset~~ shifts towards lower densities ~~y values~~ due to the core's lateral heterogeneity while the CT density still lines up well with the cuboid results. The ice contents of this cube are also much lower than CT and MSCL results. This is due to the collection procedure of the cubes which were just off-center to accommodate a duplicate run of cubes down the middle of the core for CT imaging and destructive measurements (as shown in Figure 1). This single cube highlights the ~~effect of importance of considering the differences~~ in the locations of ROIs between CT/MSCL and the cuboid methods. Moreover, at this depth in the core cuboid sample, there was a clast which resulted in a local density high and lower ice content.

In this core, the 65 μm VICs agree well with the cuboid-VICs, MSCL ($RMSE = 4\%$) ice contents, and 25 μm cube scan results ($RMSE = 3\%$) while in the transition core, the 65 μm VICs underestimated the other VIC results. The difference between the 65 μm VIC results and other VIC results for all cores except the diamict could be a result of the sample's grain size as the diamict has high clay content (~18%) relative to the other cores (~8-12%) (Table 1).

3.12.4 Ice-poor Silt Core (BH20B-337):

Figure 9 shows the results of the ice-poor silt core from both destructive (cuboid) and non-destructive (CT and MSCL) methods, illustrating a massive (non-visible) cryostructure within this inorganic silt that highlights the relatively low overall ice content throughout the core. This core has little variability throughout its profile. The CT bulk densities are consistent with both the cuboid ($RMSE = 0.14 \text{ g/cm}^3$) and gamma attenuation data ($RMSE = 0.14 \text{ g/cm}^3$) (Figure 9). The 65 μm EIC results compare well with the cuboid EIC results ($RMSE = 5\%$) while the 25 μm cube scan ice contents show strong agreement ($RMSE = 3\%$) with the volumetric cuboid ice content estimates. It should be noted that based on the EIC results of 65 μm scans, the core has a small percentage of ice (around 5%) in the form of microstructures beyond the natural pore space within the host sediment. However, upon thawing, the surrounding sediment absorbs the moisture into the available pore space, resulting in no EIC during the destructive analysis.
~~However, upon thawing, the surrounding sediment absorbs the moisture into the available pore space, resulting in no EIC during the destructive analysis.~~

3.12.5 Peat Core (DH13-589):

Figure 10 illustrates the destructive (cuboid) and non-destructive (CT and MSCL) characterization results of the peat core, with little variability throughout its profile. The core is formed of homogenous organics, with an organic-matrix cryostructure of visible ice within the densely packed peat. The CT bulk density results are similar to both the cuboid ($\text{RMSE} = 0.05 \text{ g/cm}^3$) and gamma attenuation results ($\text{RMSE} = 0.03 \text{ g/cm}^3$) (Figure 10). The $65 \text{ }\mu\text{m}$ ice content results (39-48% of EIC) are also in accordance with the cuboid excess ice results ($\text{RMSE} = 4\%$). The $65 \text{ }\mu\text{m}$ and $25 \text{ }\mu\text{m}$ VICs are both showing good estimates of VICs ($\text{RMSE} = 1\%$). It should be ~~considered that~~^{considered}~~noted that~~ the adjusted method for extraction of supernatant water, using slight pressure to release water from organic matrix, was applied to the cubes of this core. As it was previously discussed, this pressure will release the excess water that was absorbed by the peat skeleton upon thaw (Johnston, 1981).

3.23 Sensitivity analysis

In this study in order to do a sensitivity analysis and investigate the impact of resolution on the delineation between ice and sediment, repeat scans were conducted on ~~the same~~^{a same} cube. Initially, the half cores (10 cm diameter) were scanned with a $65 \text{ }\mu\text{m}$ voxel size. This was due to the physical size (width) of the imaging window. The smaller size of the cubes, however, presented an opportunity to collect data from the same material but at a resolution of $25 \text{ }\mu\text{m}$. Some of the cubes were also scanned at the same $65 \text{ }\mu\text{m}$ resolution as the half cores to make a direct comparison. Figure 11 shows the same slice location and orientation from the same cube at two different resolutions.

A ROI, shown as a red square in Figure 11, was then selected in each cube scan to make a direct comparison between the delineated (Otsu split) ice contents from image processing and the ice contents determined from the cuboid results. As reference points, the cuboid ice content results for this cube were as follows; 22% EIC and 65% VIC. Figure 12 shows the collected data from repeat image processing steps using the Otsu method of each cube as well as the cuboid results. The initial image processing steps for both the $25 \text{ }\mu\text{m}$ and $65 \text{ }\mu\text{m}$ scans closely capture the expected value of the EIC. However, only the $25 \text{ }\mu\text{m}$ cube captures a representative value relative to the cuboid data for the expected VIC. This value is reached after 6 image processing steps using the Otsu method. These results illustrate the sufficiency of $25 \text{ }\mu\text{m}$ resolution in extracting trapped ice inside pore spaces of this sandy silt sample which could be due to the smaller size of pores than the resolution. The nature of the curve suggests that VIC cannot be delineated from the $65 \text{ }\mu\text{m}$ resolution scans however EIC is possible.

~~G~~ Additionally, there is an observable increase in the amount of pore space or gas captured in the $25 \text{ }\mu\text{m}$ resolution relative to the $65 \text{ }\mu\text{m}$. This difference highlights the $25 \text{ }\mu\text{m}$ scan's increased potential to capture, and as a result segment, the different components within the scanned material.

3.34 Comparison of CT and Cuboid Density and Excess Ice Results:

Segmentation of the CT images using the Otsu method allows comparison of CT-derived bulk densities, excess ice, and volumetric ice contents with estimates from the cuboid method at similar resolution. We completed these comparisons at 65

490 μm and $25\ \mu\text{m}$ (Figures 13, 14 and 15). These figures display good agreement for density, excess ice, and volumetric ice
491 measurements with RMSE of $0.12\ \text{g}/\text{cm}^3$, 6%, and 3%, respectively. Additionally, the CT results compare well with the MSCL
492 results for both density and VIC with RMSE's of $0.08\ \text{g}/\text{cm}^3$ and 7%, respectively (Figures 16 and 17). The differences between
493 the estimated EICs from CT image processing ($65\ \mu\text{m}$ -whole core) and the measured ones from the cuboid method are due to
494 the differing resolutions, i.e., 0.5 cm for CT and 2 cm for the cuboid method, as well as the different locations of the regions
495 of interest (previously described in section 2.2). The strong accordance of the VICs highlights the opportunity for higher
496 resolution scans to estimate pore ice.

497 3.4.5 Comparison of Non-destructive Methods:

498 The results of this study show strong agreement between the two non-destructive methods: CT and MSCL and highlight the
499 importance of continued development and refinement of non-destructive methods for extracting physical properties from
500 permafrost materials.

501 The presented CT method allows for whole core high-resolution ($65\ \mu\text{m}$) three-dimensional imaging of cores,
502 measurement of bulk density and estimation of excess ice contents at a user-defined scale. This contrasts with MSCL which is
503 restricted to a fixed data collection transect down the center of the core ($\sim 1\text{cm}$ wide) with a maximum sample resolution of \sim
504 0.5 cm, high resolution ($25\ \mu\text{m}$) 2-dimensional half-core images and currently provides only volumetric ice estimates, and no
505 direct estimates of excess ice. The CT method is capable of estimating volumetric ice contents but requires cores to be
506 subsampled to a smaller size (2x2x4 cm cube) to allow for finer resolution scans ($25\ \mu\text{m}$).

507 It is worth noting that the MSCL provides a more rapid method for collecting bulk density and volumetric ice content
508 estimations in comparison with relative to the CT method. However, in addition to bulk density and volumetric ice content
509 estimations, the CT method can provide direct estimates of excess ice content. Visible ice can be segmented and isolated from
510 the remaining sediment and pore ice when scanning split cores at $65\ \mu\text{m}$ voxel size, allowing the opportunity to better estimate
511 EIC values compared to MSCL methods. Therefore, in terms of a non-destructive method for identifying and quantifying
512 excess ice within permafrost cores the CT method provides a more robust approach although the image processing and
513 acquisition costs are significantly greater.

514 4 Conclusions

515 This study investigated the application of high-resolution industrial CT scanning as a non-destructive method to tackle the
516 limitations of traditional destructive methods (e.g., visual acuity, poor reproducibility, and low resolution) in permafrost
517 characterization. Investigations were done by systematically by (e.g., visual acuity, poor reproducibility and reproducibility, and
518 low resolution) systematically logging permafrost cores, visualising cryostructures, measuring bulk density, and
519 estimating volumetric and excess ice contents, independently. Five permafrost cores, representing common materials
520 encountered in permafrost regions, were scanned at voxel sizes spatial resolutions of 65 and $25\ \mu\text{m}$. A new calibration method
521 was used to extract real densities in g/cm^3 directly from CT images. Image segmentation results using Otsu automatic image

Formatted: Font: 10 pt

Formatted: Normal, Border: Top: (No border), Bottom: (No border), Left: (No border), Right: (No border), Between : (No border)

Formatted: Font color: Auto

522 [thresholding method illustrated the effectiveness of this method in generating robust segmentation results while the visual](#)
523 [inspection method has its own drawbacks, e.g. inspector's visual acuity and poor reproducibility.](#)

524 The initial identification of different materials from CT images showed 3 classes; air (gas), ice, and sediments while image
525 processing [steps](#) of the scans [\(–using an automatic segmentation technique \(Otsu method\)](#) illustrated significant density
526 differences in ice and sediment classes. Image segmentation results using multiple image processing steps showed
527 visual/excess ice as a lower density relative to the pore ice and delineated two sediment classes based on densities.

528 Since manual and visual thresholding is subject to operator experience and judgment and also not applicable in images
529 with unimodal histograms related to materials with close densities (organic materials and ice), an automatic thresholding
530 technique was used in this study to generate more consistent results.

531 Comparison of the image processing results and extracted physical properties of 5 permafrost cores were validated
532 against a destructive method (cuboid) and MSCL non-destructive method. The results showed strong agreement between these
533 three methods (CT and cuboid) considering their differing resolutions and regions of interest with overall average RMSE's of
534 3%, 6% and 0.12 g/cm³ for VIC, EIC and density, respectively. This agreement demonstrates the applicability and reliability
535 of non-destructive methods in tracking physical and cryostructural details of permafrost cores and producing replicable, cost-
536 effective measurements.

537 A sensitivity analysis of the impact of differing resolutions on the delineation between ice and sediment showed that
538 higher resolution scans generate more accurate VICs while the lower resolution scans are still sufficient for estimation of EICs
539 and a rough estimation of VICs.

540 The proposed approach of this study will help build more robust permafrost datasets and strengthen future permafrost
541 research efforts in mapping [permafrost properties and](#) the distribution of excess ice and predicting thaw settlement. It also
542 presents an opportunity to develop methods to extract more information from existing datasets based on an acute understanding
543 of the relations between key physical permafrost properties. The next steps can be followed by [improving our understanding](#)
544 [and techniques of scanning permafrost as well as](#) using machine-learning-based image segmentation methods to generate
545 datasets and explore the relations between physical permafrost properties.

546 **Author contribution**

547 MR, JP, DF, and JH planned the project; MR, JH, and JP developed the methods; MR, JH, and JP performed the measurements;
548 MR and JH analyzed the data; MR, JP and JH wrote the manuscript draft; MR, JP, JH, and DF reviewed and edited the
549 manuscript.

550 **Competing interests**

551 The authors declare that they have no conflict of interest.

552 **Acknowledgements**

553 The authors would like to thank Evan Francis who helped with sample preparation in earlier experiments. We would also like
554 to thank Nikon Metrology for the support and constructive feedback they provided throughout the project. Casey Buchanan is
555 thanked for collecting the diamict sample used in this study.

556 **Financial support**

557 This research was supported by the NSERC funded Permafrost Partnership Network for Canada (PermafrostNet) and NSERC
558 Discovery grant to Duane Froese. Laboratory infrastructure for the Permafrost Archives Laboratory was funded by Canadian
559 Foundation for Innovation, Government of Alberta, and University of Alberta.

560 **References**

- 561 [Amato, G., Andò, E., Lyu, C., Viggiani, G., & Eiksund, G. R. \(2022\). A glimpse into rapid freezing processes in clay with x-](#)
562 [ray tomography. Acta Geotechnica, 17, 327–338. https://doi.org/10.1007/s11440-021-01201-0](#)
563 Ashi, J., Computed tomography scan image analysis of sediments, in Proc. ODP, Sci. Results, edited by Shipley, T. H., Y.
564 Ogawa, P. Blum, and J. M. Bahr, 156, 151–159, 1997.
565 Bandara, S., Froese, D. G., St. Louis, V. L., Cooke, C. A., and Calmels, F.: Postdepositional Mercury Mobility in a Permafrost
566 Peatland from Central Yukon, Canada, ACS Earth Sp. Chem., 3, 770–778,
567 https://doi.org/10.1021/acsearthspacechem.9b00010, 2019.
568 Brown, J., Ferrians, O., Heginbottom, J., and Melnikov, E. S.: Circum-Arctic map of permafrost and ground-ice conditions,
569 https://doi.org/10.3133/cp45, 1997.
570 Cai, L., Lee, H., Schanke Aas, K., and Westermann, S.: Projecting circum-Arctic excess-ground-ice melt with a sub-grid
571 representation in the Community Land Model, Cryosphere, 14, 4611–4626, https://doi.org/10.5194/tc-14-4611-2020, 2020.
572 Calmels, F. and Allard, M.: Ice segregation and gas distribution in permafrost using tomodesitometric analysis, Permafr.
573 Periglac. Process., 15, 367–378, https://doi.org/10.1002/ppp.508, 2004.
574 Calmels, F. and Allard, M.: Segregated ice structures in various heaved permafrost landforms through CT Scan, Earth Surf.
575 Process. Landforms, 33, 209–225, https://doi.org/10.1002/esp.1538, 2008.
576 Calmels, F., Clavano, W. R., and Froese, D. G.: Progress on X-ray computed tomography (CT) scanning in permafrost studies,
577 in: GeoCalgary 2010: the 63. Canadian geotechnical conference and 6. Canadian permafrost conference, Calgary, AB
578 (Canada), 12-15 Sep , 1353–1358, 2010.
579 [Ducharme, M. A., Allard, M., Côté, J., & L'Hérault, E. Measurements of permafrost thermal conductivity through CT-scan](#)
580 [analysis. the 68th Canadian Geotechnical Conference and the 7th Canadian Permafrost Conference, Québec, 20-23 Sep.](#)

581 Crory, F.: Settlement associated with the thawing of permafrost, Hanover, New Hampshire, 599–607 pp., 1973.

582 Darrow, M. M. and Lieblappen, R. M.: Visualizing cation treatment effects on frozen clay soils through μ CT scanning, Cold
583 Reg. Sci. Technol., 175, <https://doi.org/10.1016/j.coldregions.2020.103085>, 2020.

584 Duchesne, M. J., Moore, F., Long, B. F., , Labrie, J.: A rapid method for converting medical Computed Tomography scanner
585 topogram attenuation scale to Hounsfield Unit scale and to obtain relative density values. Engineering Geology 103, 100–105,
586 2009.

587 Duliu, O.: Computer axial tomography in geosciences: an overview. Earth-Sci. Rev.
588 48 (4), 265–281, 1999. [https://doi.org/10.1016/S0012-8252\(99\)00056-2](https://doi.org/10.1016/S0012-8252(99)00056-2)

589 Van Everdingen, R. O.: MULTI-LANGUAGE GLOSSARY of PERMAFROST and RELATED GROUND-ICE TERMS,
590 Calgary, 1998.

591 Harris, S. A., French, H. M., Heginbottom, J. A., Johnston, G. H., Ladanyi, B., Sego, D. C., and van Everdingen, R. O.:
592 Glossary of permafrost and related ground-ice terms, National Research Council of Canada, 1988,
593 <https://doi.org/10.4224/20386561>

594 Fan, X., Lin, Z., Gao, Z., Meng, X., Niu, F., Luo, J., Yin, G., Zhou, F., Lan, A.: Cryostructures and ground ice content in ice-
595 rich permafrost area of the Qinghai-Tibet Plateau with Computed Tomography Scanning. Journal of Mountain Science. 18.
596 1208-1221. 10.1007/s11629-020-6197-x, 2021.

597 [French, H. M.: The Periglacial Environment, Wiley, 2007, https://doi.org/10.1002/9781118684931](https://doi.org/10.1002/9781118684931)

598 Flisch, A., and Becker, A.: Industrial X-ray computed tomography studies of lake sediment drill cores. In: Mees, F., Swennen,
599 R., Van Geet, M., Jacobs, P. (Eds.), Applications of X-ray Computed Tomography. Geological Society, London, Special
600 Publication, 215, pp. 205–212, 2003. <https://doi.org/10.1144/GSL.SP.2003.215.01.19>

601 [French, H., & Shur, Y.: The principles of cryostratigraphy. Earth-Science Reviews, 101\(3-4\), 190-206, 2010.](https://doi.org/10.1016/j.earscirev.2010.04.002)
602 <https://doi.org/10.1016/j.earscirev.2010.04.002>

603

604 Gilbert, G. L., Kanevskiy, M., and Murton, J. B.: Recent Advances (2008–2015) in the Study of Ground Ice and
605 Cryostratigraphy, in: Permafrost and Periglacial Processes, 377–389, <https://doi.org/10.1002/ppp.1912>, 2016.

606 Heiri, O., Lotter, A.F. and Lemcke, G., 2001. Loss on ignition as a method for estimating organic and carbonate content in
607 sediments: reproducibility and comparability of results. Journal of paleolimnology, 25(1), pp.101-110.
608 <https://doi.org/10.1023/A:1008119611481>.

609 Hounsfield, G.N.: Computerized transverse axial scanning (tomography). Part I. Description of system. Br. J. Radiol. 46 (552),
610 1016–1022, 1973. <https://doi.org/10.1259/0007-1285-46-552-1016>

611 Johnston, G. H.: Permafrost: engineering design and construction, National Research Council Canada. Associate Committee
612 on Geotechnical Research, 1981.

Jorgenson, M. T., Macander, M., Jorgenson, J. C., Ping, C. L., and Harden, J.: Ground ice and carbon characteristics of eroding coastal permafrost at Beaufort Lagoon, northern Alaska, 495–500, 2003.

Kanevskiy, M., Shur, Y., Fortier, D., Jorgenson, M.T., Stephani, E., 2011a. Cryostratigraphy of late Pleistocene syngenetic permafrost (yedoma) in northern Alaska, Itkillik River exposure. *Quaternary Research* 75, 584–596 <http://dx.doi.org/10.1016/j.yqres.2010.12.003>, 2011.

Kanevskiy, M., Shur, Y. L., Connor, B., and Dillon, M. R.: Study of the Ice-Rich Syngenetic Permafrost for Road Design (Interior Alaska), in: Tenth International Conference on Permafrost TICOP, 191–196, 2012.

Ketcham, R. A. and Carlson, W. D.: Acquisition, optimization and interpretation of X-ray computed tomographic imagery: applications to the geosciences, *Comput. Geosci.*, 27, 381–400, [https://doi.org/10.1016/S0098-3004\(00\)00116-3](https://doi.org/10.1016/S0098-3004(00)00116-3), 2001.

Kokelj, S. V. and Burn, C. R.: Ground ice and soluble cations in near-surface permafrost, Inuvik, Northwest Territories, Canada, *Permafr. Periglac. Process.*, 14, 275–289, <https://doi.org/10.1002/ppp.458>, 2003.

Kokelj, S. V. and Jorgenson, M. T.: Advances in Thermokarst Research, *Permafr. Periglac. Process.*, 24, 108–119, <https://doi.org/10.1002/ppp.1779>, 2013.

Kozaki, T., Suzuki, S., Kozai, N., Sato, S., and Ohashi, H.: Observation of Microstructures of Compacted Bentonite by Microfocus X-Ray Computerized Tomography (Micro-CT), *J. Nucl. Sci. Technol.*, 38, 697–699, <https://doi.org/10.1080/18811248.2001.9715085>, 2001.

Knoll, G.F.: Radiation Detection and Measurement. John Wiley and Sons, New York, 1999.

Kumar and Tiwari: A Comparative Study of Otsu Thresholding and K-means Algorithm of Image Segmentation, *Int. J. Eng. Tech. Res.*, 9, 2019.

Kyle, J. R. and Ketcham, R. A.: Application of high resolution X-ray computed tomography to mineral deposit origin, evaluation, and processing, *Ore Geol. Rev.*, 65, 821–839, <https://doi.org/10.1016/j.oregeorev.2014.09.034>, 2015.

Lapalme, C. M., Lacelle, D., Pollard, W., Fortier, D., Davila, A., and McKay, C. P.: Cryostratigraphy and the Sublimation Unconformity in Permafrost from an Ultraxerous Environment, University Valley, McMurdo Dry Valleys of Antarctica, *Permafr. Periglac. Process.*, 28, 649–662, <https://doi.org/10.1002/ppp.1948>, 2017.

Lawrence, D. M., Slater, A. G., Romanovsky, V. E., and Nicolsky, D. J.: Sensitivity of a model projection of near-surface permafrost degradation to soil column depth and representation of soil organic matter, *J. Geophys. Res.*, 113, F02011, <https://doi.org/10.1029/2007JF000883>, 2008.

[Lin, Z., Gao, Z., Fan, X., Niu, F., Luo, J., Yin, G., and Liu, M.: Factors controlling near surface ground-ice characteristics in a region of warm permafrost, Beiluhe Basin, Qinghai-Tibet Plateau, *Geoderma*, 376, 114540, <https://doi.org/10.1016/j.geoderma.2020.114540>, 2020.](#)

[Murton, J. B., & French, H. M.: Cryostrutures in permafrost, Tuktoyaktuk coastlands, western arctic Canada. *Canadian Journal of Earth Sciences*, 31\(4\), 737-747. DOI:10.1139/e94-067, 1994.](#)

645 Nguyen, T. T. H., Cui, Y.-J., Ferber, V., Herrier, G., Ozturk, T., Plier, F., Puiatti, D., Salager, S., and Tang, A. M.: Effect of
 646 freeze-thaw cycles on mechanical strength of lime-treated fine-grained soils, *Transp. Geotech.*, 21, 100281,
 647 <https://doi.org/10.1016/j.trgeo.2019.100281>, 2019.
 648 Nitzbon, J., Westermann, S., Langer, M., Martin, L. C. P., Strauss, J., Laboor, S., and Boike, J.: Fast response of cold ice-rich
 649 permafrost in northeast Siberia to a warming climate, *Nat. Commun.*, 11, 2201, <https://doi.org/10.1038/s41467-020-15725-8>,
 650 2020.
 651 [Nitzbon, J., Gadylyayev, D., Schlüter, S., Köhne, J. M., Grosse, G., & Boike, J. \(2022\). Brief communication: Unravelling the](#)
 652 [composition and microstructure of a permafrost core using X-ray computed tomography. *The Cryosphere*, 16, 3507–3515.](#)
 653 <https://doi.org/10.5194/tc-16-3507-2022>
 654 [add cino viggiani](#)
 655 O'Neill, H. B. and Burn, C. R.: Physical and temporal factors controlling the development of near-surface ground ice at
 656 Illisarvik, Western Arctic coast, Canada, *Can. J. Earth Sci.*, 49, 1096–1110, <https://doi.org/10.1139/E2012-043>, 2012.
 657 Object Research Systems. Dragonfly; Object Research Systems: Montreal, QC, Canada, 2021.
 658 Otsu, N.: A Threshold Selection Method from Gray-Level Histograms, *IEEE Trans. Syst. Man. Cybern.*, 9, 62–66,
 659 <https://doi.org/10.1109/TSMC.1979.4310076>, 1979.
 660 Pumple, J., Monteath, A., Harvey, J., Roustaei, M., Alvarez, A., Buchanan, C., & Froese, D. (2024³). Non-destructive multi-
 661 sensor core logging allows rapid imaging, measurement of bulk density and estimation of ice content in permafrost
 662 cores. *EGUsphere*, 18, 2023, [489-5034–27](#). <https://doi.org/10.5194/tc-18-489-2024>[https://doi.org/10.5194/egusphere-2023-](https://doi.org/10.5194/egusphere-2023-571)
 663 [571](#)
 664 Pullman, E. R., Jorgenson, M. T., and Shur, Y.: Thaw settlement in soils of the Arctic Coastal Plain, Alaska, *Arctic, Antarct.*
 665 *Alp. Res.*, 39, 468–476, [https://doi.org/10.1657/1523-0430\(05-045\)\[PULLMAN\]2.0.CO;2](https://doi.org/10.1657/1523-0430(05-045)[PULLMAN]2.0.CO;2), 2007.
 666 Roustaei, M., Pumple, J., Harvey, J., and Froese, D.: Estimating ice and unfrozen water in permafrost samples using industrial
 667 computed tomography scanning, in: *GeoCalgary 2022*, 2022a.
 668 Roustaei, M., Pumple, J., Hendry, M. T., Palat, A., and Froese, D.: Freeze-thaw impacts on macropore structure of fiber-
 669 reinforced clay by industrial computed tomography scanning, in: *GeoCalgary 2022*, 2022b.
 670 Schramm, L. A. and Becht, M.: Estimating excess ground ice in Arctic tundra landscapes by a statistical analysis of drained
 671 thermokarst lake basins-A comparison between research sites in Alaska, *Institute of Geography, Catholic University of*
 672 *Eichstätt - Ingolstadt*, 2019.
 673 Shur, Y. L.: The upper horizon of permafrost soils, in: *Proceedings of the Fifth International Conference on Permafrost*, 867–
 674 871, 1988.
 675 Soret M, Bacharach SL, Buvat I. Partial-volume effect in PET tumor imaging. *J Nucl Med*. 2007;48:932–945.

Stephani, E., D. Fortier, Y. Shur, R. Fortier, and G. Doré. "A geosystems approach to permafrost investigations for engineering applications, an example from a road stabilization experiment, Beaver Creek, Yukon, Canada." Cold Reg. Sci. Technol. 100: 20–35. <https://doi.org/10.1016/j.coldregions.2013.12.006>, 2014.

Subcommittee, P.: Glossary of permafrost and related ground-ice terms. Associate Committee on Geotechnical Research. National Research Council of Canada, Ottawa, 156, 63-64, 1988. <https://doi.org/10.1139/e94-067>

Tanaka, E. Y., Yoo, J. H., Rodrigues, A. J., Utiyama, E. M., Birolini, D., and Rasslan, S.: A computerized tomography scan method for calculating the hernia sac and abdominal cavity volume in complex large incisional hernia with loss of domain, Hernia, 14, 63–69, <https://doi.org/10.1007/s10029-009-0560-8>, 2010.

Torrance, J. K., Elliot, T., Martin, R., and Heck, R. J.: X-ray computed tomography of frozen soil, Cold Reg. Sci. Technol., 53, 75–82, <https://doi.org/10.1016/j.coldregions.2007.04.010>, 2008.

Wang, S., Yang, P., and Yang, Z. (Joey): Characterization of freeze–thaw effects within clay by 3D X-ray Computed Tomography, Cold Reg. Sci. Technol., 148, 13–21, <https://doi.org/10.1016/j.coldregions.2018.01.001>, 2018.

Wellington, S.L., Vinegar, H.J.: X-ray computerized tomography. J. Pet. Technol. 39 (8), 885–898, 1987.

Westermann, S., Langer, M., Boike, J., Heikenfeld, M., Peter, M., Etzelmüller, B., and Krinner, G.: Simulating the thermal regime and thaw processes of ice-rich permafrost ground with the land-surface model CryoGrid 3, Geosci. Model Dev., 9, 523–546, <https://doi.org/10.5194/gmd-9-523-2016>, 2016.

Zhang, T., Barry, R. G., Knowles, K., Heginbottom, J. A., and Brown, J.: Statistics and characteristics of permafrost and ground-ice distribution in the Northern Hemisphere 1, Polar Geogr., 23, 132–154, <https://doi.org/10.1080/10889379909377670>, 1999.

706
707
708
709

710
711

Table 1: Sampling location and physical properties of cores analyzed in the study.

Core ID	Length (cm)	Classification/ Properties	Collection Location/ Depositional Environment	Clay (%)	Silt (%)	Sand (%)
BH18-211	23	Ice-rich silt	Alaska HWY, Yukon, Canada	11	66	23
BH12F-138	16	ice-rich silty peat (top) and ice-poor silt (bottom)	Alaska HWY, Yukon, Canada	top 8 bottom 12	top 52 bottom 57	top 40 bottom 31
BS19-3-6	19	Diamicton	Dempster HWY, Yukon, Canada	18	51	31
BH20B-337	20	Ice-poor silt	Alaska HWY, Yukon, Canada	8	67	25
DH13-589	26	Ice-rich homogenous peat.	Dempster HWY, Yukon, Canada	N/A	N/A	N/A

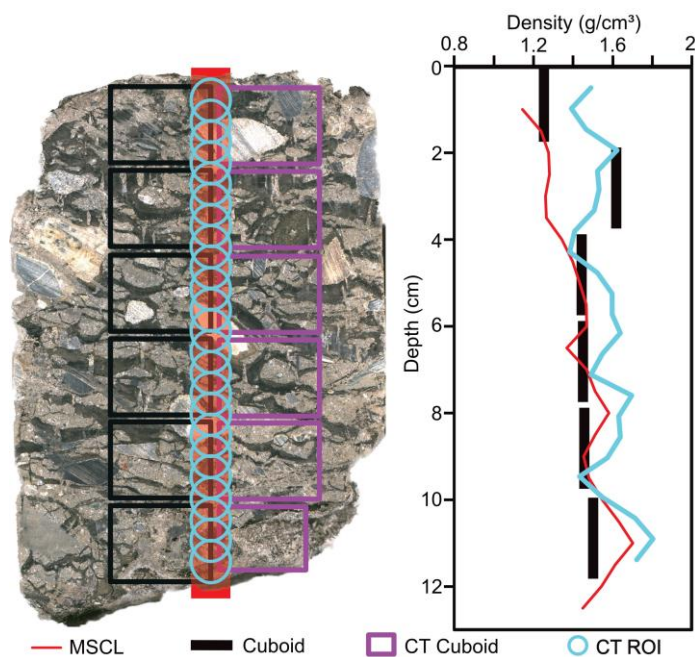


Figure 1: Image of a core highlighting the destructive subsample locations relative to the non-destructive data collection transects (black: subsampled cubes for destructive measurements, purple: subsampled cubes for CT scans).

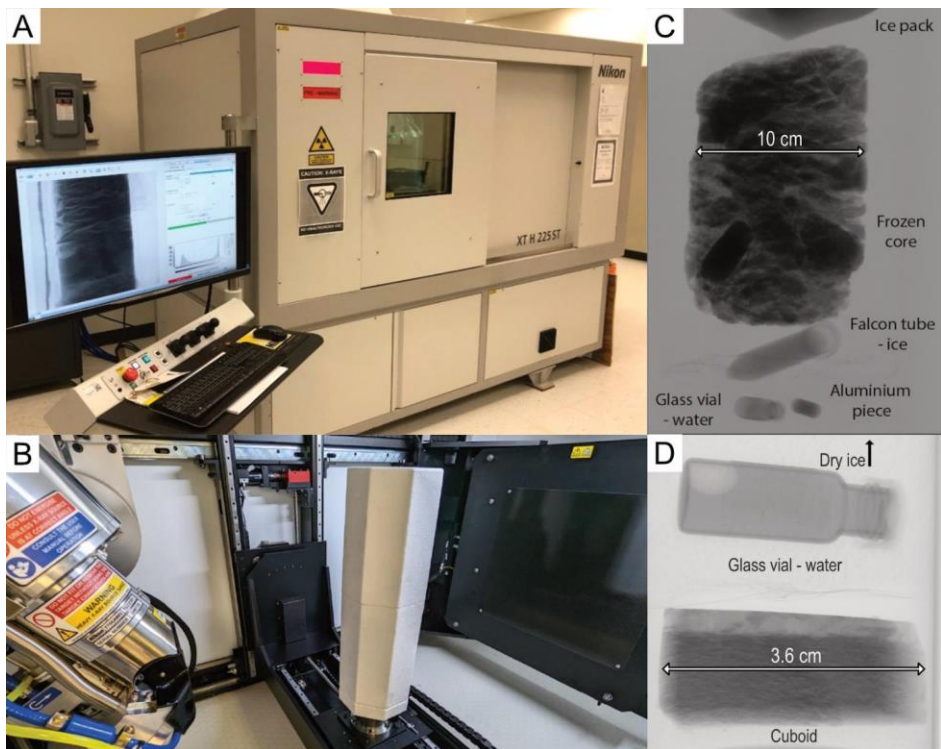
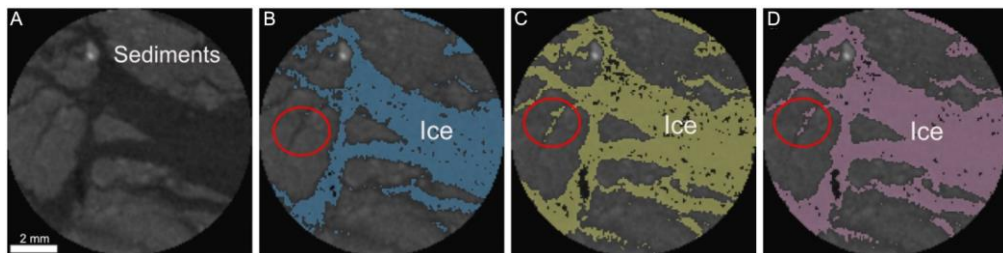
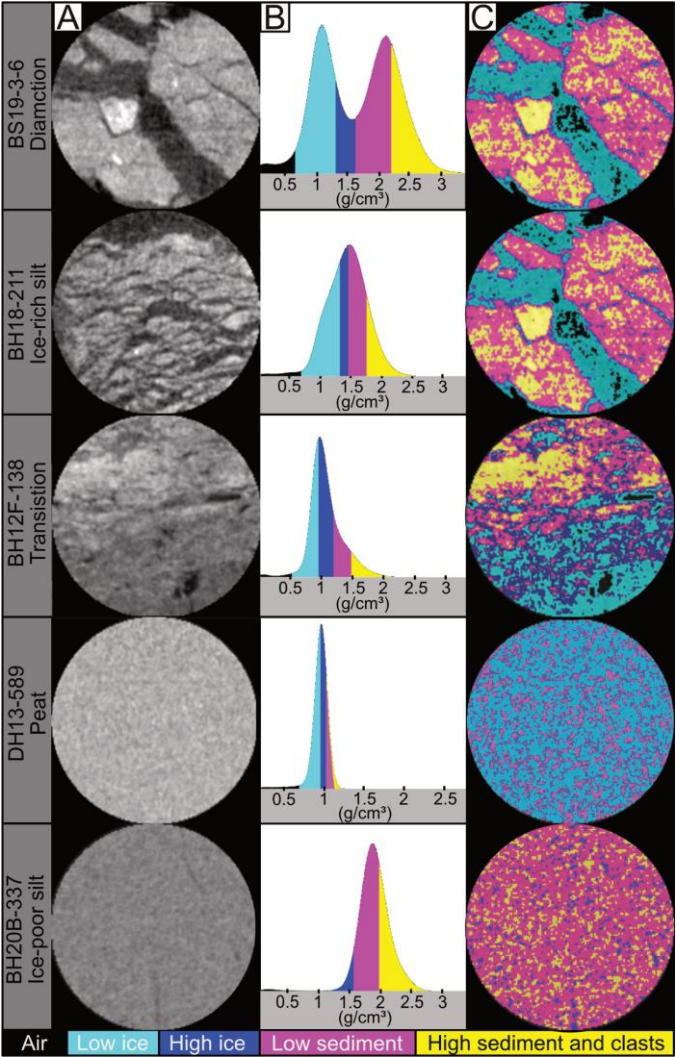


Figure 2: (A) The CT scanner of the PACS Lab.(B) The internal setup for the core scan. (C) X-ray image of the internal setup of the core (D) X-ray image of the internal setup of the cube.



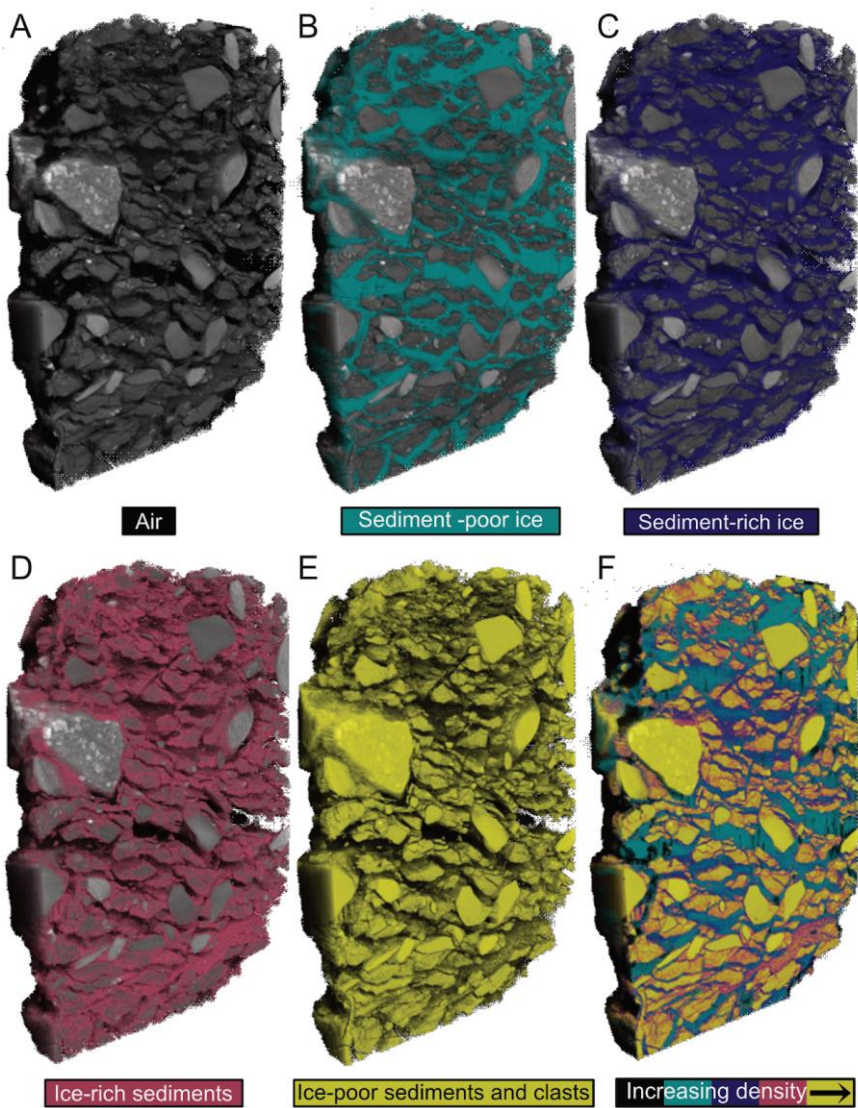
723 **Figure 3: Overview of a slice from ice rich silt core (A) before image processing (B) after the first step, (C) after the second step, and**
724 **(D) after the third step of image processing using the Otsu method.**



725

726
727

Figure 4: (A) overview of slices from the permafrost cores before image processing (B) histograms, and (C) image segmentation results



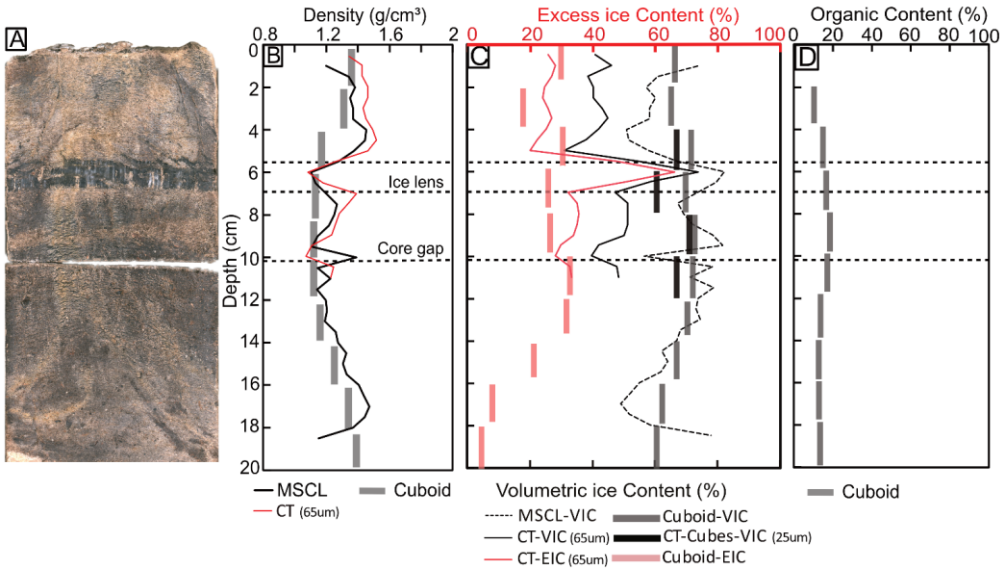
728

729
730

Figure 5: Image segmentation results of the diamicton core.
Table 1: Root mean square error results for the comparison between the CT, Cuboid and MSCL VIC, EIC and density results.

Core ID	RMSE Density CT vs Cuboid (g/cm ³)	RMSE VIC CT vs Cuboid (%)	RMSE VEIC CT vs Cuboid (%)	RMSE Density CT vs Geotek (g/cm ³)	RMSE VIC CT vs Geotek (%)
BS19-3-6	0.14	3	8	0.14	4
BH18-211	0.12	7	9	0.05	8
DH13-589	0.05	1	4	0.03	4
BH12F-138 (top)	0.07	3	7	0.02	11
BH12F-138 (bottom)	0.19	3	2	0.10	10
BH12F-138 (whole core)	0.13	3	5	0.06	10
BH20B-337	0.14	3	5	0.14	3
Overall average	0.12	3	6	0.08	7

731
732



733
734
735

Figure 6: (A) MSCL image of the ice-rich, organic-rich silt core; (B) bulk density; (C) ice contents; (D) organic content distribution in core depth; (E) black and white image of MSCL image with ice highlighted in black.

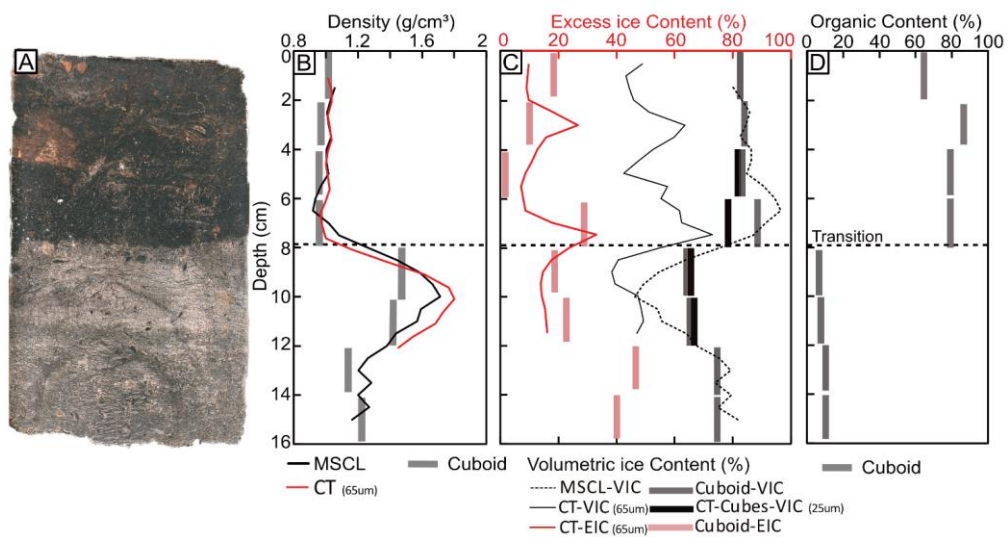


Figure 7: (A) MSCL image of the transition core; (B) bulk density; (C) ice contents; (D) organic content distribution in core depth; (E) black and white image of MSCL image with ice highlighted in black.

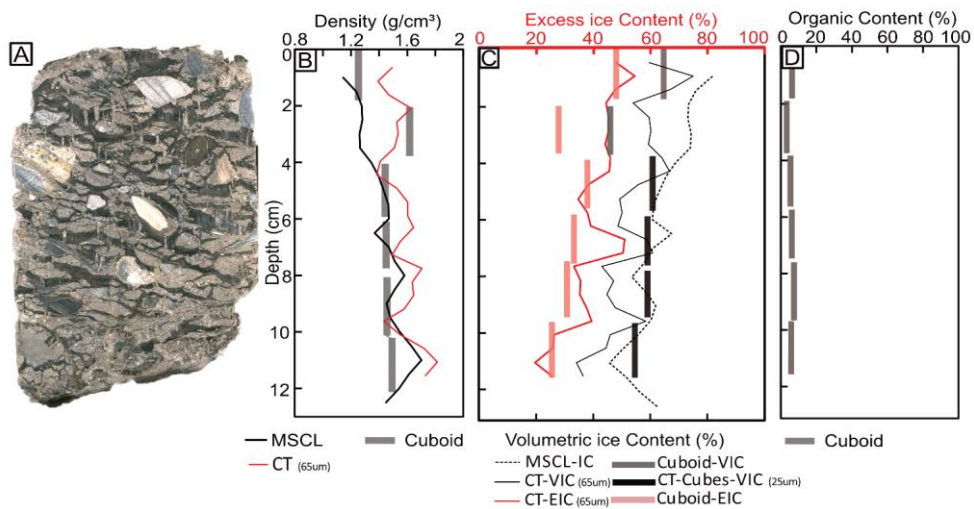


Figure 8: (A) MSCL image of the diamicton core; (B) bulk density; (C) ice contents; (D) organic content distribution in core depth; (E) black and white image of MSCL image with ice highlighted in black.

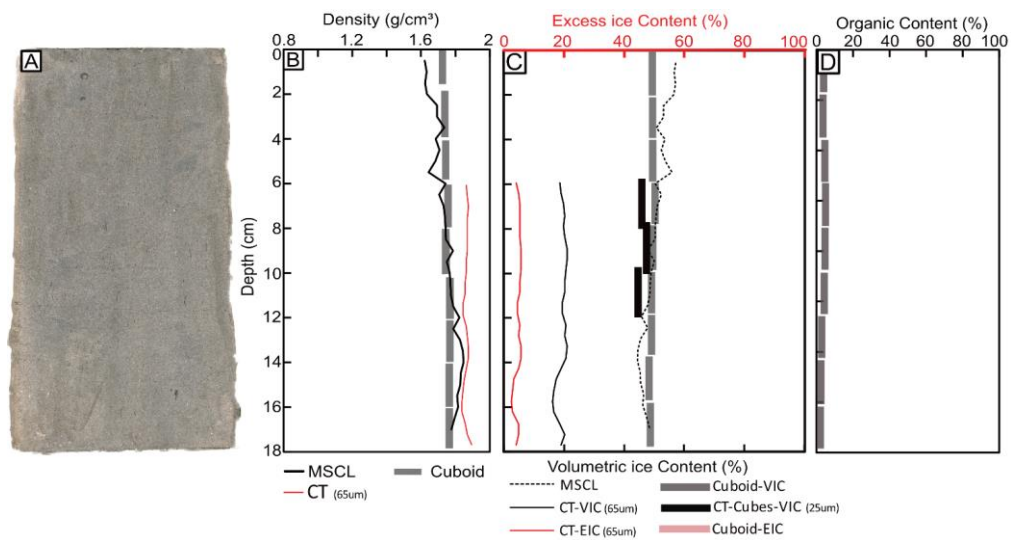


Figure 9: (A) MSCL image of the ice-poor silt core; (B) bulk density; (C) ice contents; (D) organic content distribution in core depth; (E) black and white image of MSCL image with ice highlighted in black.

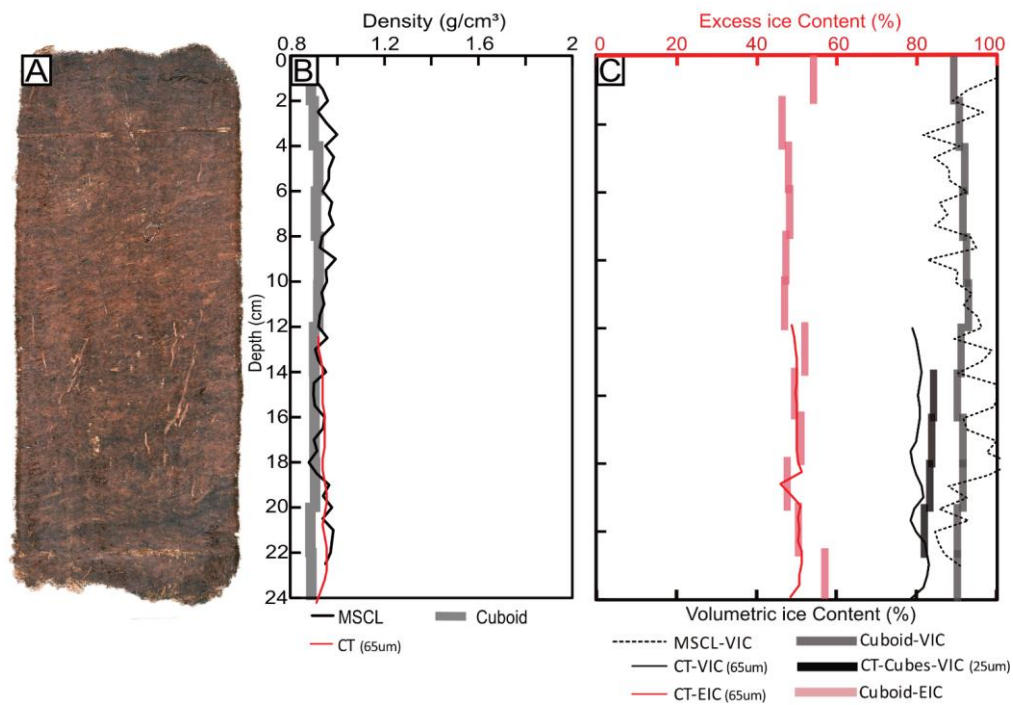


Figure 10: (A) MSCL image of the peat core; (B) bulk density; (C) ice contents; (D) organic content distribution in core depth; (E) black and white image of MSCL image with ice highlighted in black.

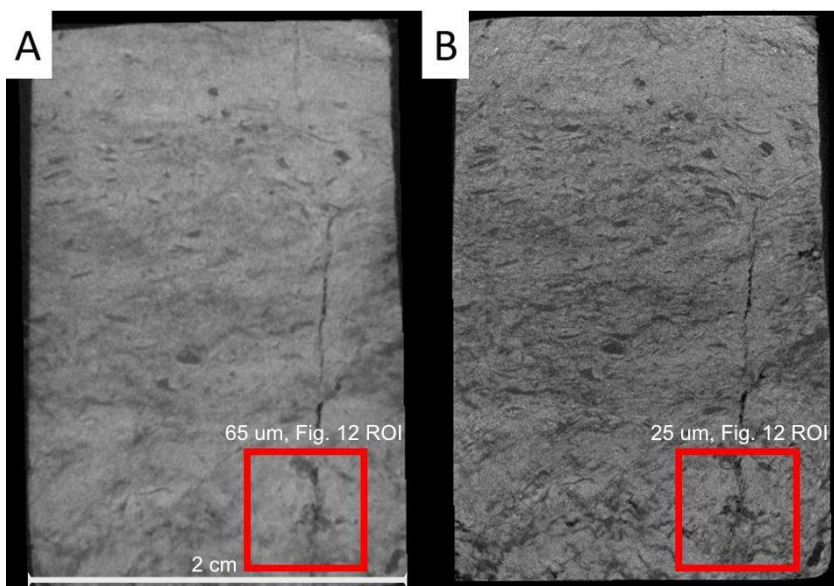


Figure 11: CT images of a cube (BH12F-138-10-12 cm) from the transition core at 65 μm (A) and 25 μm (B).

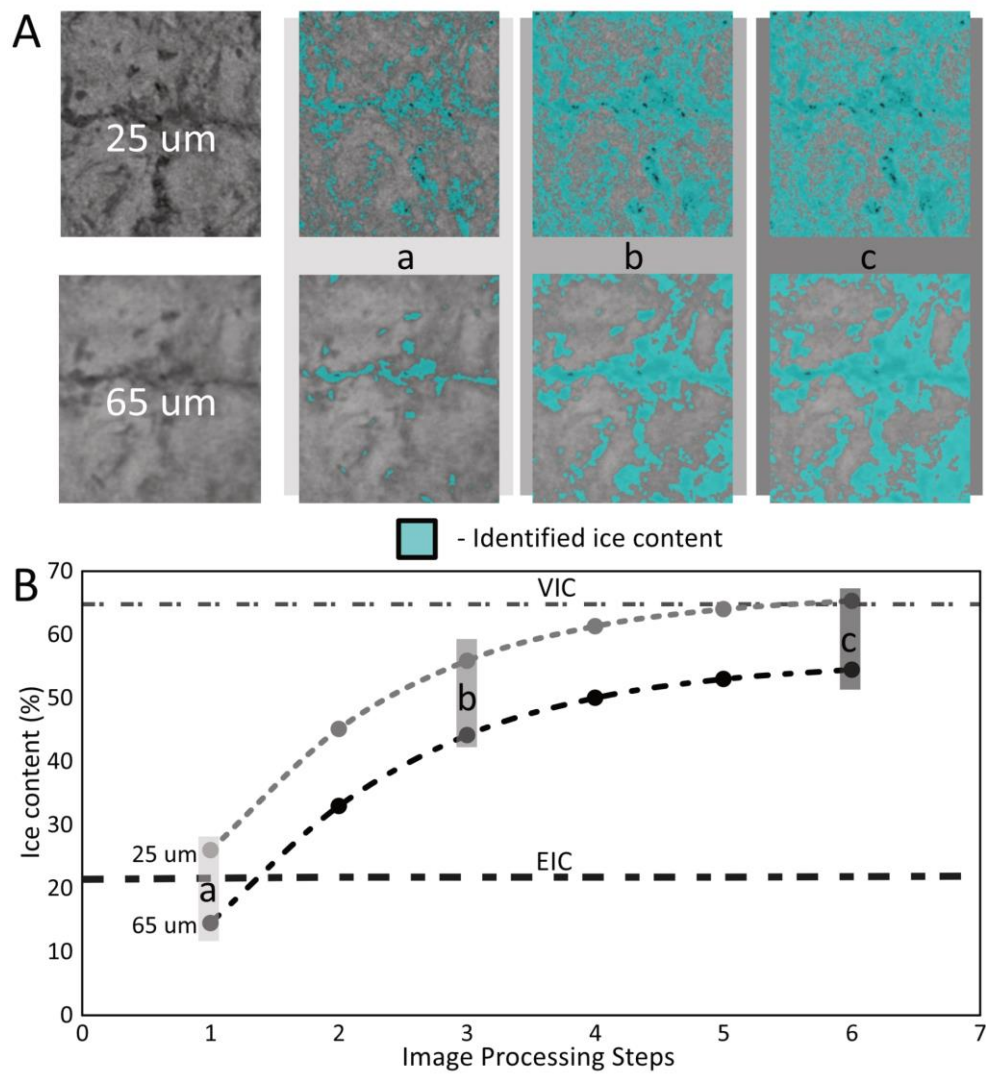


Figure 12: (A) CT ROI's taken from the 65 μm and 25 μm cube scans (BH12F-138-10-12 cm), (B) Identified ice contents at each image processing step using the Otsu split method.

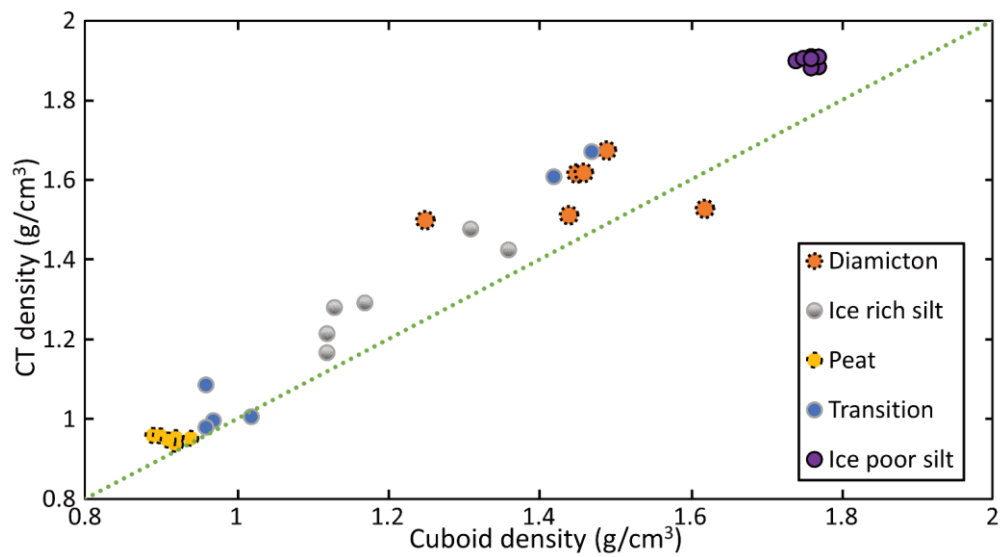


Figure 13: Estimated densities from CT image processing vs calculated ones from cuboid method.

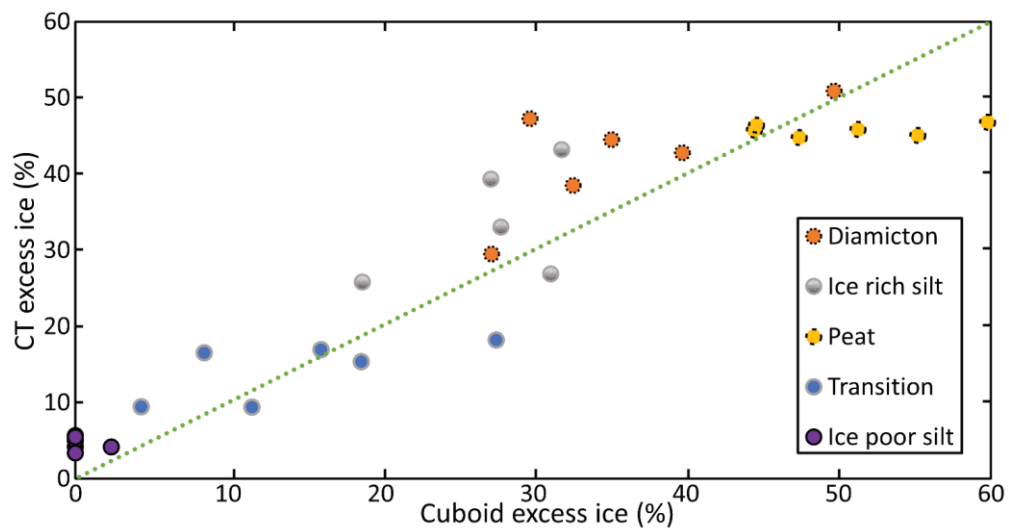


Figure 14: Estimated excess ice contents from CT image processing vs calculated values from cuboid method.

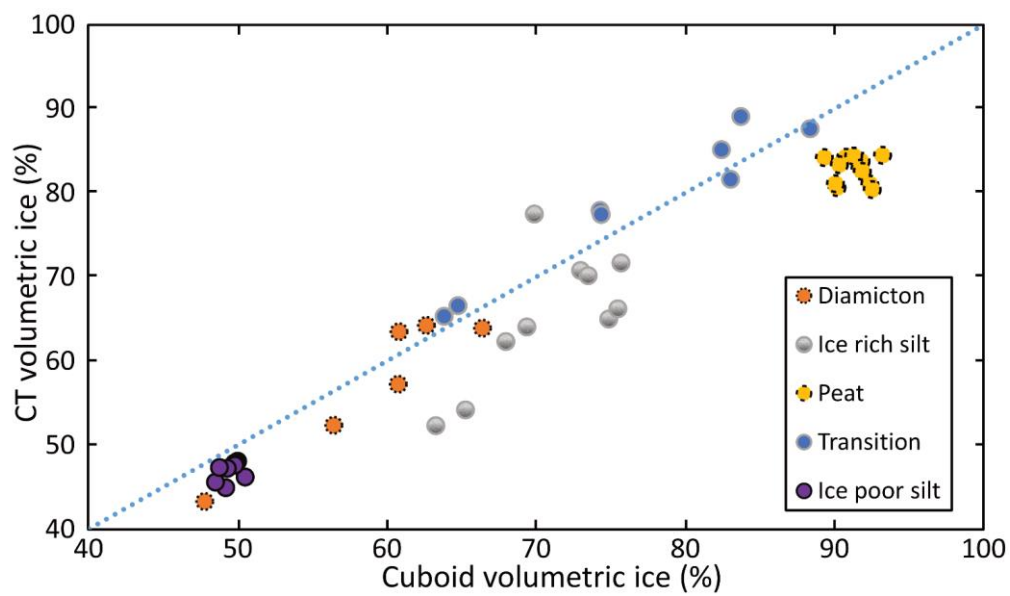


Figure 15: Estimated volumetric ice contents from CT image processing vs calculated values from cuboid method.

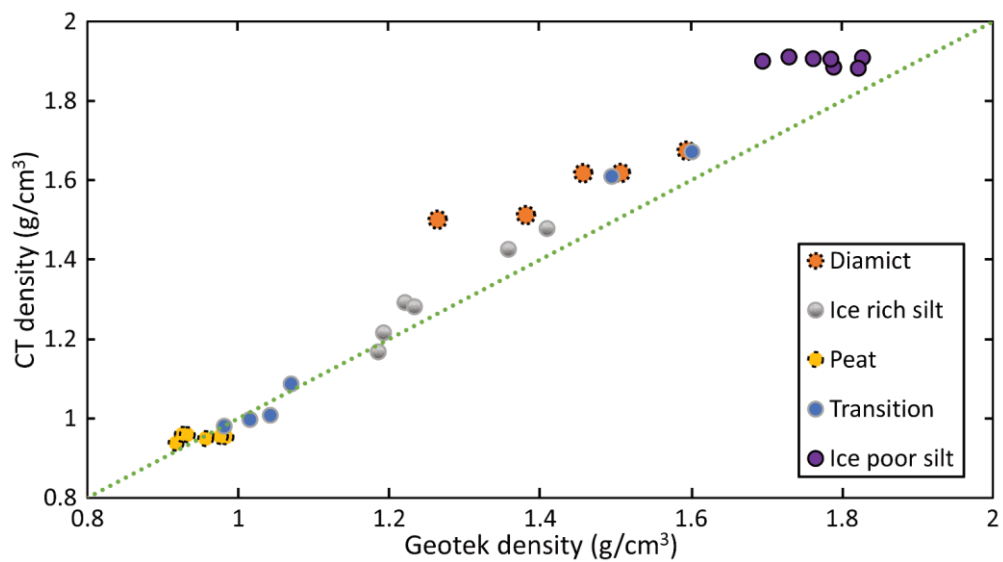


Figure 16: Estimated bulk density from CT image processing vs calculated values from MSCL method.

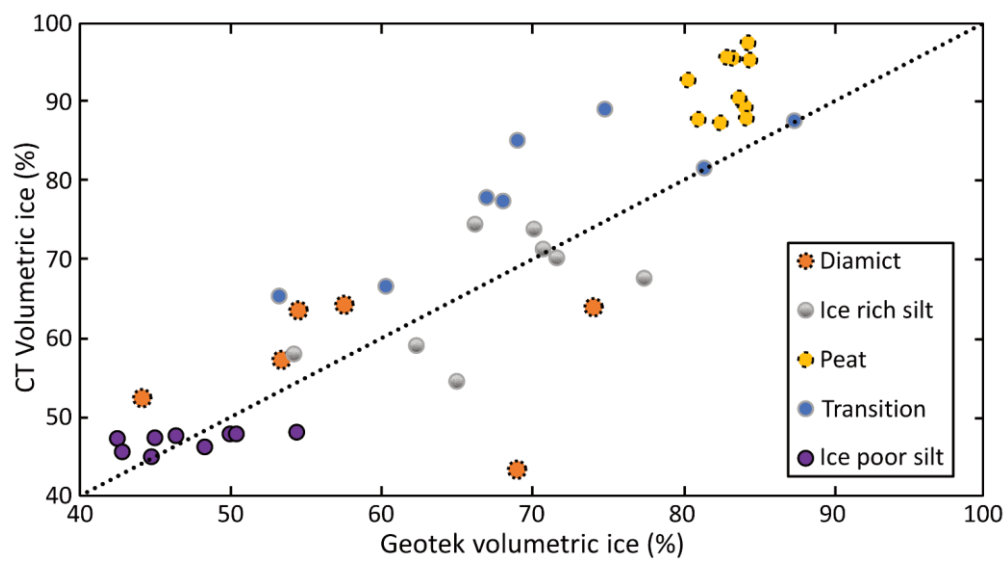


Figure 17: Estimated volumetric ice contents from CT image processing vs calculated values from MSCL method.